Anomalous Chained Turbulence in Actively Driven Flows on Spheres

Anomalous Chained Turbulence in Actively Driven Flows on Spheres

Oscar Mickelin,[1] Jonasz Słomka,[1] Keaton J. Burns,[2] Daniel Lecoanet,[3] Geoffrey M. Vasil,[4] Luiz M. Faria,[1] and Jörn Dunkel[1]

[1]*Department of Mathematics, Massachusetts Institute of Technology, Cambridge, Massachusetts 02139-4307, USA*
[2]*Department of Physics, Massachusetts Institute of Technology, Cambridge, Massachusetts 02139-4307, USA*
[3]*Princeton Center for Theoretical Science, Princeton University, Princeton, New Jersey 08544, USA*
[4]*School of Mathematics and Statistics, University of Sydney, Sydney, New South Wales 2006, Australia*

(Received 16 October 2017; published 20 April 2018)

Recent experiments demonstrate the importance of substrate curvature for actively forced fluid dynamics. Yet, the covariant formulation and analysis of continuum models for nonequilibrium flows on curved surfaces still poses theoretical challenges. Here, we introduce and study a generalized covariant Navier-Stokes model for fluid flows driven by active stresses in nonplanar geometries. The analytical tractability of the theory is demonstrated through exact stationary solutions for the case of a spherical bubble geometry. Direct numerical simulations reveal a curvature-induced transition from a burst phase to an anomalous turbulent phase that differs distinctly from externally forced classical 2D Kolmogorov turbulence. This new type of active turbulence is characterized by the self-assembly of finite-size vortices into linked chains of antiferromagnetic order, which percolate through the entire fluid domain, forming an active dynamic network. The coherent motion of the vortex chain network provides an efficient mechanism for upward energy transfer from smaller to larger scales, presenting an alternative to the conventional energy cascade in classical 2D turbulence.

DOI: 10.1103/PhysRevLett.120.164503

Substrate geometry profoundly affects dynamics and energy transport in complex fluids flowing far from equilibrium [1–3]. Examples range from magnetohydrodynamic turbulence on stellar surfaces [1] to the rich microscale dynamics of topological defects in active nematic vesicles [2,3]. Studying the interplay between spatial curvature and actively driven fluid flows is also essential for understanding microbial locomotion [4], biofilm formation [5] and bioremediation [6] in soils [7], tissues [8], and water [9–11]. Over the past two decades, important breakthroughs have been made in characterizing active-stress driven matter flows in planar Euclidean geometries both theoretically [12–15] and experimentally [16–18]. More recently, theoretical work has begun to focus on incorporating curvature effects into active matter models [19–25]. Despite some promising progress, the hydrodynamic description of pattern-forming nonequilibrium liquids in non-Euclidean spaces continues to pose conceptual challenges, attributable to the difficulty of formulating exactly solvable continuum models and devising efficient spectral methods in curved geometries.

Aiming to help improve upon these two issues, we introduce and investigate here the covariant extension of a generalized Navier-Stokes (GNS) model [26–29] describing incompressible active fluid flow on an arbitrarily curved surface. Focusing on a spherical "bubble" geometry, we derive exact stationary solutions and numerically explore the effects of curvature on the steady-state flow dynamics, using the open-source spectral code Dedalus [30]. The numerically obtained phase diagrams, energy spectra, and flux curves predict an anomalous turbulent phase when the spectral bandwidth of the active stresses becomes sufficiently narrow. This novel type of 2D turbulence supports an unexpected upward energy transfer mechanism, mediated by the large-scale collective dynamics of self-organized vortex chains, akin to actively moving antiferromagnetic spin chains. At high curvature, the anomalous turbulence transforms into a quasistationary burst phase, whereas for broadband spectral forcing the flow dynamics transitions to classical 2D Kolmogorov turbulence, accumulating energy in a few large-scale vortices. We next motivate and define the covariant GNS model for an arbitrary 2D surface; analytical and numerical results for the sphere case will be discussed subsequently.

Recent experiments have investigated the collective dynamics of swimming bacteria [16] and algae [31] in thin quasi-2D soap films held by a coplanar wire frame. Generalizing to non-Euclidean geometries [2,3], which can be realized with soap bubbles or curved wire frames [32], we consider here a freestanding nonplanar 2D film in which the fluid flow is driven by active stresses, as in suspensions of swimming bacteria [33,34] or ATP-driven microtubule networks [35,36]. On a curved manifold, the fluid velocity field components v^a satisfy incompressibility and Cauchy momentum conservation [37,38],

$$\nabla_a v^a = 0, \tag{1a}$$

$$\partial_t v^a + v^b \nabla_b v^a = \nabla^a \sigma + \nabla_b T^{ab}, \tag{1b}$$

where $\nabla_b v^a$ denotes the covariant derivative of v^a, $a, b = 1, 2$ and σ is the (surface) tension. The stress tensor T^{ab} includes passive and active contributions from the solvent fluid viscosity and the stresses exerted by the microswimmers on the fluid. Below, we study the covariant version of the linear active-stress model [26–29]

$$T^{ab} = f(\nabla^2)(\nabla^a u^b + \nabla^b u^a),$$
$$f(\nabla^2) = \Gamma_0 - \Gamma_2 \nabla^2 + \Gamma_4 \nabla^2 \nabla^2, \tag{1c}$$

where $\nabla^2 = \nabla^a \nabla_a$ is the tensor Laplacian. In qualitative agreement with experimental observations for active suspensions [16,18,36,39], the polynomial ansatz for f in Eq. (1c) generates vortices of characteristic size Λ and growth time τ, provided that $\Gamma_2 < 0$, which introduces a bandwidth κ of linearly unstable modes [28]. General mathematical stability considerations demand $\Gamma_0, \Gamma_4 > 0$. The phenomenological model defined in Eq. (1) is minimal in the sense that it assumes the active stresses create to leading order a linear instability, while neglecting energy transfer within the active component. As verified in Ref. [29], the linear active-stress model, Eq. (1c), suffices to quantitatively reproduce the experimentally measured velocity distributions and flow correlations in 3D bacterial [18] and ATP-driven microtubule [36] suspensions. More generally, closely related GNS models have also been studied in the context of soft-mode turbulence and seismic waves [26,27]. Numerical solutions of the GNS Eqs. (1) show significant phenomenological similarities with magnetohydrodynamic (MHD) flows driven by electromagnetic stresses [40], suggesting that the results below may also apply to astrophysical systems.

Exact stationary solutions of Eqs. (1) for a sphere of radius R can be constructed from the vorticity-stream function formulation (Supplemental Material [41])

$$\Delta \psi = -\omega, \tag{2a}$$

$$\partial_t \omega + \{\omega, \psi\} = f(\Delta + 4K)(\Delta + 2K)\omega, \tag{2b}$$

where ψ and ω are the stream function and vorticity. The advection term in spherical coordinates (θ, ϕ) reads $\{\omega, \psi\} = (\partial_\theta \omega \partial_\phi \psi - \partial_\phi \omega \partial_\theta \psi)/(R^2 \sin\theta)$. $K = R^{-2}$ is the Gaussian curvature and Δ the standard spherical Laplacian. Since the spherical harmonics Y_ℓ^m diagonalize the Laplacian, $\Delta Y_\ell^m = -R^{-2}\ell(\ell+1)Y_\ell^m$ for integers ℓ, m such that $\ell \geq 0$ and $|m| \leq \ell$, an arbitrary superposition

$$\psi = \sum_{|m| \leq \ell} \psi_{m\ell} Y_\ell^m \tag{3}$$

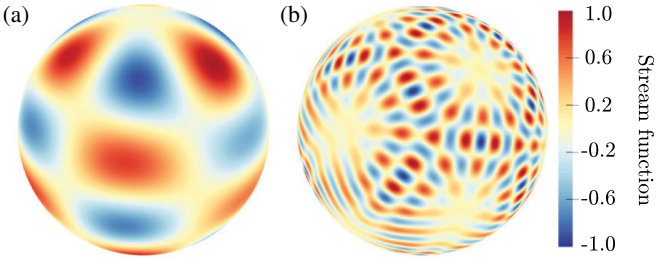

FIG. 1. Stationary solutions of Eqs. (2) are superpositions of the form Eq, (3) with $f[-\ell(\ell+1)+4] = 0$. (a) An exact stationary solution with $\ell = 6$ which is also approximately realized as a transient state in the time-dependent burst solution of Fig. 2 (movie 1). (b) Complex symmetric solutions can be constructed by choosing the expansion coefficients $\psi_{m\ell}$ accordingly [46]. In both panels, the stream functions are normalized by their maxima; see Supplemental Material [41] for coefficients $\psi_{m\ell}$.

solves the system Eq. (2) exactly, provided that the eigenvalue ℓ is an integer root of $f[-\ell(\ell+1)+4] = 0$ (Supplemental Material [41]). As usual, the velocity field is tangent to the level sets of the stream function. Two particular exact solutions are shown in Fig. 1. The first example, Fig. 1(a), is reminiscent of the square lattice solutions found earlier in the flat 2D case [28]. The second example in Fig. 1(b) illustrates a flow field with fivefold symmetry, obtained by applying the superposition procedure of Ref. [46]. Although these exact solutions are not stable, they provide some useful intuition about the instantaneous flow patterns expected in dynamical simulations (Fig. 2), similar to exact coherent structures [47] in conventional turbulence [48].

To find and analyze time-dependent solutions of Eqs. (1), we performed numerical simulations using Dedalus [30], an open-source framework for solving differential equations with spectral methods. The Eqs. (1) were solved directly as a coupled partial differential-algebraic system for the scalar tension σ and vector velocity v^a. To spatially discretize the system, we used spin-weighted spherical harmonics, which are a parameterized family of basis functions that correctly capture the analytical behavior of spin-weighted functions on the sphere (Supplemental Material [41]). Under this spectral expansion, the system Eq. (1) is reduced to a set of coupled ordinary differential-algebraic equations for the time evolution of the expansion coefficients. We solve these equations using mixed implicit-explicit time stepping, in which the linear terms of the evolution equations are integrated implicitly, the linear constraints are enforced implicitly, and the nonlinear terms are integrated explicitly. This allows us to simultaneously evolve the velocity field while enforcing the incompressibility constraint, and with a time step that is limited by the advective Courant-Friedrichs-Lewy time condition rather than the diffusive time at any scale.

The parameters $(\Gamma_0, \Gamma_2, \Gamma_4)$ in Eqs. (1) define a characteristic time scale τ, a characteristic vortex diameter

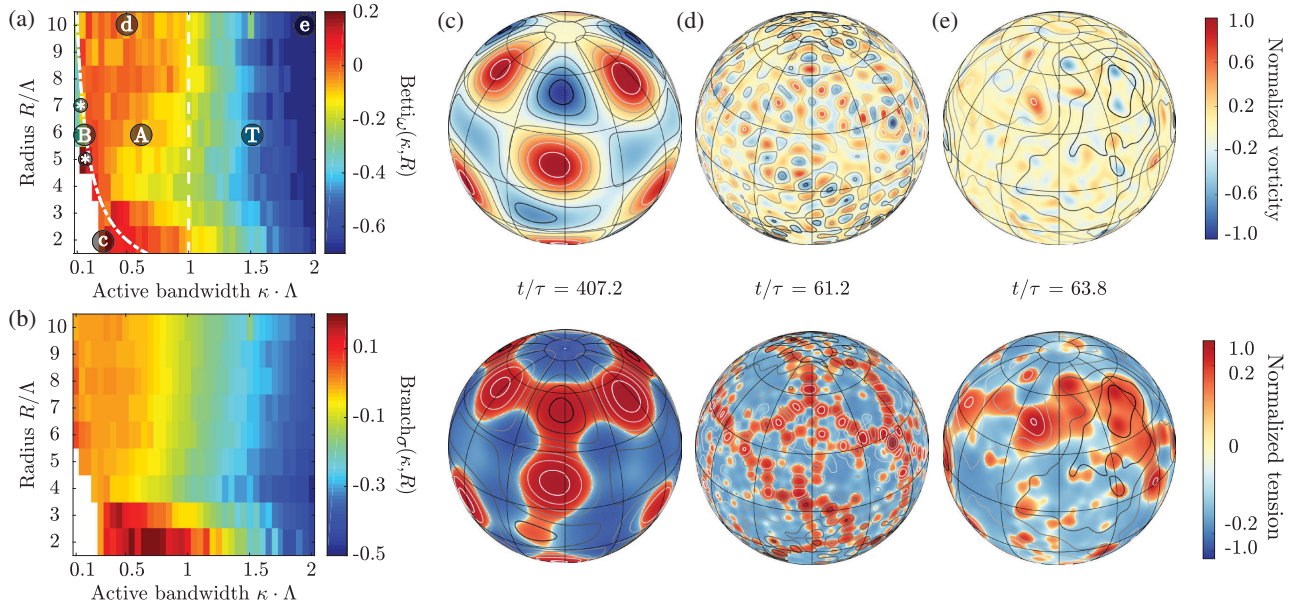

FIG. 2. Phase diagrams [(a),(b)] and representative still images [(c)–(e)] from simulations showing quasistationary burst dynamics (B phase), anomalous vortex-network turbulence (A phase), and classical 2D turbulence (T phase). (a), (b) The A and T phase are approximately separated by the condition $\kappa\Lambda = 1$ (vertical dashed line) and differ by the average number of vortices (a), the branch geometry of the tension field (b), and the energy spectra (Fig. 3). The B phase arises for narrow-band energy injection $\kappa R \lesssim 1$ when only a single ℓ mode is active (region right below the dash-dotted line); decreasing κ further gives a passive fluid (white region). (c)–(e) Top: Instantaneous vorticity fields normalized by their maxima. Bottom: Surface tension fields normalized by the maximum deviation from the mean. (c) Quasistationary preburst state from movie 1 resembling the exact solution in Fig. 1(a); see movies 2 and 3 for additional examples labeled by $*$ in panel (a). (d) For subcritical curvature and intermediate energy injection bandwidths, $R^{-1} < \kappa < \Lambda^{-1}$, the flows develop a percolating vortex-chain network structure (movie 4), with accumulation of tension and vorticity along the edges. (e) For broadband energy injection $\kappa\Lambda > 1$, smaller eddies merge to create larger vortices, as typical of classical 2D turbulence (movie 5). Parameters: (a) $\alpha_\omega = 0.5$; (c) $R/\Lambda = 2$, $\tau = 4.9$ s, $\kappa\Lambda = 0.29$; (d) $R/\Lambda = 10$, $\tau = 14.9$ s, $\kappa\Lambda = 0.5$; (e) $R/\Lambda = 10$, $\tau = 11.7$ s, $\kappa\Lambda = 2.0$. Panels (a),(b) show steady-state time averages over $[50\tau, 100\tau]$. Solid curves in (c)–(e) indicate stream lines of the velocity fields.

Λ, and a characteristic spectral bandwidth κ, which can be directly inferred from experimental data [29]; explicit expressions are derived in the Supplemental Material [41]. Given a sphere of radius R, fixing (τ, Λ, κ) uniquely determines the parameters $(\Gamma_0, \Gamma_2, \Gamma_4)$. To explore the interplay between curvature and activity, we run 351 simulations, using $R/\Lambda \in [2, 10]$ and $\kappa \cdot \Lambda \in [0.1, 2.0]$. Typical vortex diameters for bacterial and microtubule suspensions are $\Lambda \sim 50$–100 μm with τ of the order of seconds [16,18,36,39]. Time steps were in the range $[5 \times 10^{-4}\tau, 5 \times 10^{-3}\tau]$ with a total simulation time 100τ, allowing the system to fully develop its dynamics after an initial relaxation phase during which active stresses inject energy until the viscous dissipation and activity balance on average. In the remainder, it will be convenient to regard Λ as reference length and compare the flow topologies across the (κ, R) parameter plane.

Our simulations reveal three qualitatively distinct flow regimes (Fig. 2): a quasistationary burst phase for $\kappa R \lesssim 1$ [domain B in Fig. 2(a); movies 1–3], an anomalous turbulence for $R^{-1} < \kappa < \Lambda^{-1}$ [domain A in Fig. 2(a); movie 4], and normal 2D turbulence for $\kappa\Lambda > 1$ [domain T in Fig. 2(a); movie 5]. Representative vorticity and tension fields from the corresponding steady-state dynamics are shown in Figs. 2(c)–2(e).

In the B phase, the energy injection bandwidth κ is close to the wave number spacing set by the sphere curvature R^{-1}, leaving only a single active wave number ℓ. Decreasing κ further completely suppresses active modes resulting in globally damped fluid motion [white domain in Fig. 2(a)]. The B phase is characterized by the formation of intermittent quasistationary flow patterns that lie in the vicinity of the exact stationary solutions, Eq. (3), cf. Fig. 1(a) and Fig. 2(c). Once formed, the amplitude of these flow patterns grows exponentially (Fig. S3) until nonlinear advection becomes dominant and eventually causes energy to be released through a rapid burst. Afterwards, the dynamics becomes quasilinear again with the flow settling into a new quasistationary pattern. These burst cycles are continuously repeated (movies 1–3).

The two turbulent phases A and T in Fig. 2(a) can be distinguished through topological, geometric, and spectral measures. We demonstrate this by determining the topology of the vorticity fields, the geometry of the high-tension domains, and the energy spectra for each simulation after flows had reached the chaotic steady state.

To study the vortex topology, we fix a threshold $\alpha_\omega \in [0,1]$ and identify regions in which the vorticity is larger (or smaller) than α_ω times the maximum (or minimum) vorticity (Supplemental Material [41]). This thresholding divides the sphere into patches of high absolute vorticity (Fig. S1). The number of connected domains, given by the zeroth Betti number, counts the vortices in the system. For a fixed pair (κ, R), we denote the vortex number at time t by $N_\omega(\kappa, R; t)$. Although more sophisticated methods for vortex detection exist [49], the thresholding criterion proved to be sufficient for our analysis (Fig. S2). To normalize vortex numbers across the parameter space, we fix a reference value $\kappa_* = 0.3/\Lambda$. With this, we can define a normalized Betti number as

$$\mathrm{Betti}_\omega(\kappa, R) = \frac{\langle N_\omega(\kappa, R; t) - N_\omega(\kappa_*, R; t)\rangle}{\langle N_\omega(\kappa_*, R; t)\rangle}, \qquad (4)$$

where the time average $\langle\cdots\rangle$ is taken after the initial relaxation period. Intuitively, large values of Betti_ω indicate many vortices of comparable circulation, whereas small values suggest the presence of a few dominant eddies. The variation of Betti_ω in the (κ, R)-parameter plane is color coded in Fig. 2(a). In the anomalous turbulent A phase, vortices of diameter $\approx\Lambda$ eventually cover the surface of the sphere, with stronger vortices forming chains of antiferromagnetic order [Fig. 2(d) top; movie 4]. By contrast, in the T phase characterized by broadband energy injection $\kappa > \Lambda^{-1}$, smaller eddies merge to create a small number of larger vortices, as typical of classical 2D turbulence [50] [Fig. 2(e) top; movie 5]. Interestingly, the A phase shares phenomenological similarities with the low-entropy states found in quasi-2D superfluid models [51], while the vortex condensation in the T phase corresponds approximately to the negative "temperature" regime in Onsager's statistical hydrodynamics [52]. Moreover, the upper region of Fig. 2(a), which corresponds to the small-curvature limit $R/\Lambda \gg 1$, suggests that the two phases extend to planar geometries, provided boundary effects remain negligible.

To obtain a more detailed geometric characterization of the turbulent A and T phases, we next consider the corresponding tension fields. Analogously to the case of vorticity above, we focus on regions where the local tension $\sigma(t, \boldsymbol{x})$ is larger than the instantaneous global mean value. For each connected component of the identified high-tension regions, we denote by A its total area and by ∂A its total boundary area in pixels. The ratio $\partial A/A$ is a measure of chainlike structures in the tension fields, a large value signaling a highly branched structure, whereas smaller values indicate less branching. Denoting the instantaneous sum of the ratios $\partial A/A$ over all connected high-tension domains by $A_\sigma(\kappa, R; t)$, a normalized branching index can then be defined by (Supplemental Material [41])

$$\mathrm{Branch}_\sigma(\kappa, R) = \frac{\langle A_\sigma(\kappa, R; t) - A_\sigma(\kappa_*, R; t)\rangle}{\langle A_\sigma(\kappa_*, R; t)\rangle}, \qquad (5)$$

where the time average is again taken after the initial relaxation. As evident from the phase diagram in Fig. 2(b) and the corresponding tension fields in Figs. 2(d) and 2(e), and movies 4 and 5, the geometric characterization confirms the existence of an anomalous turbulent phase, in which vortices combine to form percolating dynamic networks with high tension being localized along the edges [Fig. 2(d) bottom; movie 4].

To compare the energy transport in the anomalous turbulent phase with classical 2D turbulence, we analyze the energy spectra and fluxes for the A and T phases. Expanding in spherical harmonics, $\psi = \sum_{m,\ell} \psi_{m\ell} Y_\ell^m$, the energy of mode ℓ is $E(\ell) = \sum_{|m|\le\ell} \ell(\ell+1)|\psi_{m\ell}|^2$. The corresponding mean energy flux across ℓ in the statistically stationary state is obtained as (Supplemental Material [41])

$$\Pi(\ell) = -2\sum_{\ell'\ge\ell} f[4-\ell'(\ell'+1)][2-\ell'(\ell'+1)]\langle E_{\ell'}\rangle, \qquad (6)$$

where f is the polynomial defined in Eq. (1c). Figure 3 shows the numerically obtained energy spectra $E(\ell)$ and fluxes $\Pi(\ell)$ for four active bandwidths κ. In all four cases, the kinetic energy produced in the injection range

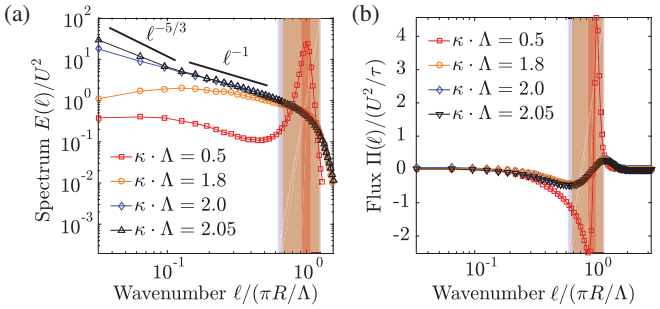

FIG. 3. Time-averaged energy spectra and fluxes indicate two qualitatively different types of upward energy transport. (a) For narrow-band energy injection $\kappa\Lambda < 1$, the energy spectrum exhibits a peak corresponding to the dominant vortex size Λ (red curve). For broadband injection $\kappa\Lambda \sim 2$, the spectra decay monotonically (blue and black curves). (b) In all four examples, the fluxes confirm inverse energy transport, albeit with different origins. For broadband energy injection (blue and black curves), the upward energy flux to larger scales is due to vortex mergers [Fig. 2(e); movie 5]. By contrast, for narrow-band injection (red curve), a relatively stronger upward energy flux arises from the collective motion of vortex chains [Fig. 2(d); movie 4]. The shaded regions indicate the energy injection ranges with colors matching those of the corresponding curves, respectively. Parameters: $R/\Lambda = 10$ for a unit sphere, $\tau = 11.7$ s, time step $5\times10^{-4}\tau$, total simulation time 500τ. Spectra and fluxes were determined after relaxation by averaging over $[150\tau, 500\tau]$. For $\kappa\Lambda \gg 1$, energy steadily accumulates at larger scales and the absence of a large-scale dissipative mechanism leads to a divergent total enstrophy and kinetic energy on the sphere.

($\ell \sim \pi R/\Lambda$) propagates to both large ($\ell < \pi R/\Lambda$) and small ($\ell > \pi R/\Lambda$) scales, as indicated by negative and positive values of $\Pi(\ell)$, respectively. Energy transfer to large scales is a prominent feature of classical 2D turbulence [50,53,54] and our results show that it also occurs in active turbulence. However, the transfer mechanisms can be dramatically different, as already implied by the preceding analysis of the vorticity and tension fields. For broadband spectral forcing $\kappa\Lambda \gg 1$, the classical 2D turbulence picture of vortex mergers and energy condensation at large scales prevails [Fig. 2(e); movie 3]. For $\kappa\Lambda \lesssim 2$ the spectrum follows a k^{-1} scaling, indicating the formation of a dilute-vortex system [55]. For even larger values of κ, additional large-scale dissipation is needed to bound the upward energy transfer, in which case the spectrum is expected to approach the Kolmogorov $k^{-5/3}$ scaling [50]. By contrast, for narrow-band driving $\kappa\Lambda \lesssim 1$, the upward energy transfer is realized through the coherent motion of high-tension vortex chains. Interestingly, only this anomalous type of inverse energy cascade appears to persist in 3D active bulk fluids [29], where it is sustained by spontaneous chiral symmetry breaking [56].

In summary, we have presented analytical and numerical solutions for generalized Navier-Stokes equations describing actively driven nonequilibrium flows on a sphere. Our calculations predict that spectrally localized active stresses can induce a novel turbulent phase, in which finite-size vortices self-organize into chain complexes of antiferromagnetic order that percolate through the surface [57]. The collective motion of these chain networks enables a significant upward energy transport and may thus provide a basis for efficient fluid mixing in quasi-2D active and magnetohydrodynamic flows. Future generalizations to rotating spheres could thus promise insights into pattern formation in planetary and stellar atmospheres [58].

D. L. is supported by a Princeton Center for Theoretical Science Fellowship, and a Lyman Spitzer Jr. Fellowship. G. M. V. acknowledges support from The Australian Research Council Project No. DE140101960. This work was supported by an Alfred P. Sloan Research Fellowship (J. D.), an Edmund F. Kelly Research Award (J. D.), NSF Grant No. CBET-1510768 (J. S. and J. D.) and a James S. McDonnell Foundation Complex Systems Scholar Award (J. D.).

O. M. and J. S. contributed equally to this work. O. M. performed the numerical simulations and J. S. the analytical calculations. K. J. B, D. L., and G. M. V. developed the numerical simulations.

[1] S. Cranmer and A. van Ballegooijen, Astrophys. J. Suppl. Ser. **156**, 265 (2005).
[2] F. C. Keber, E. Loiseau, T. Sanchez, S. J. DeCamp, L. Giomi, M. J. Bowick, M. C. Marchetti, Z. Dogic, and A. R. Bausch, Science **345**, 1135 (2014).
[3] R. Zhang, Y. Zhou, M. Rahimi, and J. J. de Pablo, Nat. Commun. **7**, 13483 (2016).
[4] O. Sipos, K. Nagy, R. Di Leonardo, and P. Galajda, Phys. Rev. Lett. **114**, 258104 (2015).
[5] Y.-W. Chang, A. A. Fragkopoulos, S. M. Marquez, H. D. Kim, T. E. Angelini, and A. Fernandez-Nieves, New J. Phys. **17**, 033017 (2015).
[6] K. Das and A. K. Mukherjee, Bioresour. Technol. **98**, 1339 (2007).
[7] H. C. Bold, Bulletin of the Torrey Botanical Club **76**, 101 (1949).
[8] J. W. Costerton, P. S. Stewart, and E. P. Greenberg, Science **284**, 1318 (1999).
[9] E. Rosenberg, R. Legmann, A. Kushmaro, R. Taube, E. Adler, and E. Z. Ron, Biodegradation **3**, 337 (1992).
[10] M. Rosenberg, FEMS Microbiol. Lett. **262**, 129 (2006).
[11] E. Rosenberg, E. F. DeLong, S. Lory, E. Stackebrandt, and F. Thompson, in *The Prokaryotes* (Springer, Berlin, Heidelberg, 2013), pp. 201–214.
[12] M. C. Marchetti, J. Joanny, S. Ramaswamy, T. Liverpool, J. Prost, M. Rao, and R. A. Simha, Rev. Mod. Phys. **85**, 1143 (2013).
[13] C. W. Wolgemuth, Biophys. J. **95**, 1564 (2008).
[14] D. Saintillan and M. J. Shelley, Phys. Fluids **20**, 123304 (2008).
[15] T. Brotto, J.-B. Caussin, E. Lauga, and D. Bartolo, Phys. Rev. Lett. **110**, 038101 (2013).
[16] A. Sokolov, I. S. Aranson, J. O. Kessler, and R. E. Goldstein, Phys. Rev. Lett. **98**, 158102 (2007).
[17] M. Wu, J. W. Roberts, S. Kim, D. L. Koch, and M. P. DeLisa, Appl. Environ. Microbiol. **72**, 4987 (2006).
[18] J. Dunkel, S. Heidenreich, K. Drescher, H. H. Wensink, M. Bär, and R. E. Goldstein, Phys. Rev. Lett. **110**, 228102 (2013).
[19] L. M. Janssen, A. Kaiser, and H. Löwen, Sci. Rep. **7**, 5667 (2017).
[20] G. Salbreux and F. Jülicher, Phys. Rev. E **96**, 032404 (2017).
[21] S. Henkes, M. C. Marchetti, and R. Sknepnek, arXiv:1705.05166.
[22] D. Khoromskaia and G. P. Alexander, New J. Phys. **19**, 103043 (2017).
[23] F. Alaimo, C. Köhler, and A. Voigt, Sci. Rep. **7**, 5211 (2017).
[24] Y. Fily, A. Baskaran, and M. F. Hagan, Soft Matter **10**, 5609 (2014).
[25] Y. Fily, A. Baskaran, and M. F. Hagan, Phys. Rev. E **91**, 012125 (2015).
[26] I. A. Beresnev and V. N. Nikolaevskiy, Physica (Amsterdam) **66D**, 1 (1993).
[27] M. I. Tribelsky and K. Tsuboi, Phys. Rev. Lett. **76**, 1631 (1996).
[28] J. Słomka and J. Dunkel, Phys. Rev. Fluids **2**, 043102 (2017).
[29] J. Słomka and J. Dunkel, Proc. Natl. Acad. Sci. U.S.A. **114**, 2119 (2017).
[30] K. J. Burns, G. M. Vasil, J. S. Oishi, D. Lecoanet, B. P. Brown, and E. Quataert (to be published).
[31] J. S. Guasto, K. A. Johnson, and J. P. Gollub, Phys. Rev. Lett. **105**, 168102 (2010).
[32] R. E. Goldstein, J. McTavish, H. K. Moffatt, and A. I. Pesci, Proc. Natl. Acad. Sci. U.S.A. **111**, 8339 (2014).

[33] E. Lauga and T. R. Powers, Rep. Prog. Phys. **72**, 096601 (2009).
[34] K. Drescher, J. Dunkel, L. H. Cisneros, S. Ganguly, and R. E. Goldstein, Proc. Natl. Acad. Sci. U.S.A. **108**, 10940 (2011).
[35] S. Ramaswamy, Annu. Rev. Condens. Matter Phys. **1**, 323 (2010).
[36] T. Sanchez, D. T. N. Chen, S. J. DeCamp, M. Heymann, and Z. Dogic, Nature (London) **491**, 431 (2012).
[37] L. E. Scriven, Chem. Eng. Sci. **12**, 98 (1960).
[38] R. Aris, *Vectors, Tensors and the Basic Equations of Fluid Mechanics* (Dover Publications, Inc., New York, 1989).
[39] C. Dombrowski, L. Cisneros, S. Chatkaew, R. E. Goldstein, and J. O. Kessler, Phys. Rev. Lett. **93**, 098103 (2004).
[40] G. M. Vasil and M. G. P. Cassell (to be published).
[41] See Supplemental Material at http://link.aps.org/supplemental/10.1103/PhysRevLett.120.164503 which contains Refs. [42–45], for details of derivations and numerical implementation.
[42] G. Schwarz, *Hodge Decomposition—A Method for Solving Boundary Value Problems* (Springer-Verlag, Berlin, 1995).
[43] E. Delay, Manuscr. Math. **123**, 147 (2007).
[44] A. L. Besse, *Einstein Manifolds* (Springer Science & Business Media, New York, 2007).
[45] V. I. Arnold and B. A. Khesin, *Topological Methods in Hydrodynamics* (Springer Science & Business Media, New York, 1999), Vol. 125.
[46] W. Prandl, P. Schiebel, and K. Wulf, Acta Crystallogr. Sect. A **52**, 171 (1996).
[47] F. Waleffe, J. Fluid Mech. **435**, 93 (2001).
[48] F. Waleffe, in *Turbulence and Interactions*, edited by M. Deville, T. H. Lê, and P. Sagaut, Notes on Numerical Fluid Mechanics and Multidisciplinary Design, Vol. 105 (Springer, Berlin, Heidelberg, 2009).
[49] M. Jiang, R. Machiraju, and D. Thompson, in *The Visualization Handbook*, edited by C. D. Hansen and C. R. Johnson (Academic Press, New York, 2011).
[50] G. Boffetta and R. E. Ecke, Annu. Rev. Fluid Mech. **44**, 427 (2012).
[51] T. Simula, M. J. Davis, and K. Helmerson, Phys. Rev. Lett. **113**, 165302 (2014).
[52] L. Onsager, Nuovo Cimento Suppl. **6**, 279 (1949).
[53] R. H. Kraichnan and D. Montgomery, Rep. Prog. Phys. **43**, 547 (1980).
[54] S. Sukoriansky, B. Galperin, and N. Dikovskaya, Phys. Rev. Lett. **89**, 124501 (2002).
[55] T. Kusumura, H. Takeuchi, and M. Tsubota, J. Low Temp. Phys. **171**, 563 (2013).
[56] L. Biferale, S. Musacchio, and F. Toschi, Phys. Rev. Lett. **108**, 164501 (2012).
[57] A. Doostmohammadi, T. N. Shendruk, K. Thijssen, and J. M. Yeomans, Nat. Commun. **8**, 15326 (2017).
[58] L. N. Fletcher *et al.*, Science **319**, 79 (2008).